CHAPTER 3 HIGH THROUGHPUT CHARACTERIZATION OF TWO OTHER MATERIAL SYSTEMS: $La_{0.5}Sr_{0.5}CoO_{3+\delta}$ AND PLATINUM - $Sr_{0.06}Nb_{0.06}Bi_{1.87}O_3$

3.1 Summary

This chapter describes characterization results obtained from thin film microelectrodes of two other material systems: $La_{0.5}Sr_{0.5}CoO_{3+\delta}$ (LSC), and a composite of metal and doped bismuth oxide (platinum - $Sr_{0.06}Nb_{0.06}Bi_{1.87}O_3$). Some background about these systems is given in Section 3.2. The experimental preparation of these samples is detailed in Section 3.3. Electrochemical pathways and the corresponding equivalent circuits are described in Section 3.4. Results and discussion are presented for $La_{0.5}Sr_{0.5}CoO_{3+\delta}$ (LSC) in Section 3.5, and for platinum on $Sr_{0.06}Nb_{0.06}Bi_{1.87}O_3$ in Section 3.6. Overall conclusions are given in Section 3.7.

3.2 Two material systems

The cathode materials used in state-of-the-art solid oxide fuel cells typically fall into three categories:

(1) $La_{1-x}Sr_xMnO_3$, often with a small amount of A-site deficiency

(2) Perovskites or double-perovskites that contain Sr and Co

(3) doped Bi_2O_3

The first category, cathodes based on $La_{1-x}Sr_xMnO_3$ (LSM), was discussed in the previous chapter. In the second category, cells with a peak power density greater than 1 W/cm^2 at 600˚C (using H_2 as the fuel) have been reported using cathodes containing $Ba_{0.5}Sr_{0.5}Co_{0.8}Fe_{0.2}O_{3-\delta}$ (BSCF),[37,38] $Sm_{0.6}Sr_{0.4}CoO_{3-\delta}$ (SSC),[39] $La_{0.58}Sr_{0.4}CoO_{3-\delta}$ (LSC),[40] $PrBa_{0.5}Sr_{0.5}Co_{1.5}Fe_{0.5}O_{3-\delta}$ (PBSCF),[41] and $Sr_{0.5}Co_{0.9}Nb_{0.1}O_{3-\delta}$ (SCN).[42] In the third category, it is not as widely recognized that doped Bi_2O_3 is electrochemically active for oxygen reduction, however cells with peak power density greater than 1 W/cm^2 at 650˚C have been reported using a composite cathode of $Er_{0.4}Bi_{1.6}O_3$ - $Bi_2Ru_2O_7$.[43] In light of their high activity and relevance in applications, representative materials from the second and third categories are studied in this chapter. The selected materials are $La_{0.5}Sr_{0.5}CoO_3$ and metal-$Sr_{0.06}Nb_{0.06}Bi_{1.87}O_3$.

3.2.1 $La_{0.5}Sr_{0.5}CoO_3$

There is a general consensus that $La_{0.5}Sr_{0.5}CoO_3$ (LSC) and similar compositions are quite catalytically active for the oxygen electro-reduction reaction $O_2 + 4e^- = 2O^{2-}$. The absolute magnitude of the surface activity varies substantially between reports, however, and the stability of the activity is also not well-understood. Some studies simply state that the activity of LSC films degrades substantially over a period of tens of hours;[33,44-46] in other studies stability is implied but not explored.[47-49] There is also disagreement about the redox behavior of LSC films. One metric for the reducibility of a non-stoichiometric oxide is the chemical capacitance C_{chem}:

$$C_{chem} = \frac{-8e^2V}{k_BTV_m}\frac{\partial\delta}{\partial(\ln\left(pO2/atm\right))} \tag{3}$$

where e is the charge of an electron, V is sample volume, V_m is molar volume, k_B is Boltzmann's constant, T is temperature, δ is oxygen non-stoichiometry, and pO_2 is oxygen partial pressure. If decreasing the oxygen partial pressure causes a large increase in δ, then C_{chem} is large; thus C_{chem} can be considered a measure of how easily a material is reduced. By this metric, some researchers report that LSC films are less reducible than bulk samples,[50] while others find the opposite.[11]

3.2.2 $Sr_{0.06}Nb_{0.06}Bi_{1.87}O_3$

The catalytic activity of doped bismuth oxides towards oxygen reduction is much less widely recognized than in perovskites containing manganese or cobalt. In fact, doped bismuth oxides as cathodes were largely ignored in two recent reviews of solid oxide fuel cell materials.[51,52] The high activity was first reported in 1983, however, when Verkerk *et al.* observed an electrode resistance "many times lower" for metal-$Er_xBi_{2-x}O_3$ cathodes than for comparable metal-$Gd_{0.10}Ce_{0.90}O_2$ cathodes.[53] They also observed that the surface exchange resistance of platinum electrodes on doped zirconia and ceria substrates exhibited a minimum at roughly 10^{-2} atm O_2, whereas platinum electrodes on doped bismuth oxide substrates exhibited no such minimum. And, they observed that the activation energies obtained from sputtered gold electrodes and sputtered platinum electrodes were comparable on doped bismuth oxide but very different on doped zirconia or doped ceria. Based on these observations, they concluded that doped bismuth oxide has enough catalytic activity that the catalysis is limited by oxygen adsorption and/or diffusion on the oxide surface, not on adjacent metal surfaces, even if the metal is platinum. Follow-up studies reached similar conclusions.[54]

Many dopants have been explored, because in pure Bi_2O_3 the high-ionic-conductivity (face centered cubic) δ phase is stable only in the range 729°C - 824°C. Above that range the material melts; below that range the material converts to a monoclinic α phase with much lower ionic conductivity, a transition that involves a large volume change that typically leads to severe cracking. In general increasing the dopant concentration lowers both the phase transition temperature and the ionic conductivity.[55,56]

However, the activity of doped bismuth oxide is not accurately known for any combination of dopants. The stability of these compounds is also not clearly understood, although in many cases, a slow degradation in transport rates has been observed when the materials are annealed for many days, and in some cases this degradation has been correlated with either a slow phase transformation, cation ordering, anion ordering, and/or cation exsolution.[57]

Here a new composition is measured, $Sr_{0.06}Nb_{0.06}Bi_{1.87}O_3$, to determine its activity and to assess its stability.

3.3 Experimental details

3.3.1 Target preparation

A PLD target with nominal composition $La_{0.5}Sr_{0.5}CoO_3$ was prepared in-house by mixing the appropriate ratios of $La_2(CO_3)_2$*7.8H_2O (Alfa 99.9%), $SrCO_3$ (Aldrich 99.9%), and CoO (Alfa 99.998%) using a mortar and pestle and then sintering 10 h at 1250°C.

Substrates (10 mm x 10 mm x 1 mm) and PLD targets (25 mm diameter) with nominal compositions $Y_{0.5}Bi_{1.5}O_3$ (YB) and $Sr_{0.06}Nb_{0.06}Bi_{1.87}O_3$ (SNB) were prepared by the group of Professor Kuan-Zong Fung at the National Central University of Taiwan. According to that group, the pellets were prepared by mixing the appropriate ratios of Bi_2O_3, Y_2O_3, $SrCO_3$, and Nb_2O_5 by ball milling for 24 h, sieving with 325 mesh, calcining at 850°C (YB) or 750°C (SNB), ball milling again, uniaxial pressing, isostatic pressing, sintering at 950°C (YB) or 850°C (SNB), and then grinding and polishing to a mirror finish using alumina grit.

No unexpected reflections were detected by XRD for any of these targets. The cation ratio in a representative YB pellet was measured by EDS; it precisely matched the expected ratio. The LSC target appeared to have some porosity, roughly 30% - 50%.

3.3.2 Film preparation

Using the above targets, $La_{0.5}Sr_{0.5}CoO_3$ films were grown on (100) single crystal $Y_{0.15}Zr_{1.85}O_{1.93}$ (YSZ, 8 mol% Y_2O_3-stabilized ZrO_2) substrates by Shingo Maruyama using pulsed laser deposition at the University of Maryland. For LSC the growth used a KrF excimer laser (248 nm, ~ 0.5 J cm^{-2}, 5 Hz), a growth pressure of 30 mtorr O_2, a substrate temperature of 640°C (measured with a pyrometer), a calculated deposition rate of 2.3 nm/min, and a cooling rate of ~100°C. During all growth steps, the substrate backsides were adhered to a stage with silver paste, which was subsequently scraped off.

The as-grown LSC films were characterized by x-ray diffraction (XRD, Bruker D8 Discover, Cu Kα) and atomic force microscopy (AFM, Digital Instruments Nanoscope III). Patterning was carried out by spin coating photoresist onto the film surface (Microchemicals AZ P4620), then exposing the resist through a photomask, developing the resist, ion milling for ~45 min (milling depth of ~ 350 nm), and stripping of the residual resist. The films were characterized again after patterning by AFM and optical microscopy.

Platinum microelectrodes were fabricated on top of an SNB pellet via photolithography and d.c. magnetron sputtering. In the photolithography step, the pellet was rinsed and treated for 3 min with a 150 W oxygen plasma, then exposed for 5 min to air saturated with the adhesion promoter hexamethyldisilazane (MicroChemicals), dehydration baked at 120˚C for 5 min, spin-coated with photoresist (Shipley 1813, 2500 rpm, 30 s), baked at 115˚C for 150 s, exposed for 60 s to UV radiation (275 W, 385 nm) through a photomask, developed by immersion in MF-319 (Microposit) for 50 s, rinsed in deionized water, and treated for an additional 3 min with an oxygen plasma. The sputtering system (AJA International, Pt target, 99.99% purity) had a base pressure of 10^{-6} torr, 3 mtorr Ar working pressure, and a d.c. plasma power of 150 W. Deposited metal layers were ~600 nm thick. The microelectrode diameters were varied from 500 μm to 30 μm.

3.3.3 Impedance characterization

Each substrate was adhered to a ~ 2 cm^2 x 0.6 mm alumina sheet (McMaster) using silver paste (DAD-87, Shanghai Research Institute), which also served as a counter electrode. The paste was fired in a quartz tube under stagnant air at 600˚C - 700˚C for 1 h. A given substrate was then installed in the scanning impedance probe, and impedance spectra were acquired using zero bias, an a.c. perturbation voltage of 10 mV - 30 mV, and a frequency range of 10 kHz - 16 mHz. For the LSC measurements, a Paliney7 probe tip (American Probe & Technologies, 20 μm tip radius) was used. For SNB a $Pt_{0.7}Ir_{0.3}$ tip (Moser, 10 μm tip radius) was used. The latter tip sometimes created visible scratches in the microelectrodes; when that was observed, no further measurements were performed on the damaged microelectrode. The impedance analyzer calibration was verified before each experiment using Faraday-cage-shielded test circuits comprised of precision megaohm resistors and nanofarad capacitors. After fitting the resulting spectra, the resistance and capacitance values of the circuit components were reproduced with < 3% error.

The film temperature ranges used were 520˚C - 615˚C (for LSC) and 575˚C - 650˚C (for SNB). The oxygen partial pressure in the chamber was typically varied over the range 10^{-3} atm - 1 atm by flowing bottled dry oxygen or oxygen-nitrogen mixtures. Often a small number of representative microelectrodes were repeatedly measured at a given condition over a few hours to verify stability, after which many other microelectrodes were measured once. For the primary LSC sample reported below, a total of 680 impedance spectra were acquired over 125 h of measurement time; for SNB, 1,371 impedance spectra were acquired over 240 h.

The acquired impedance spectra were fit to various impedance expressions (derived in Section 3.3) by complex nonlinear least squares using a Matlab routine implemented in collaboration with Chris Kucharczyk. The fit residual of each complex impedance datum was weighted by the complex modulus of that datum, which serves as a proxy for the unknown variance of the datum. A few spectra had unreasonably large confidence intervals for the resulting fit parameters; these spectra were excluded.

After impedance testing, the samples were coated with ~ 10 nm carbon (Cressington 108) and characterized with a scanning electron microscope (SEM, Zeiss 1550 VP) using either in-lens or below-lens secondary electron detectors, as well as an energy dispersive spectrometer (EDS, Oxford X-Max SDD).

3.4 Electrochemical models

Different material systems can have different catalytic pathways for oxygen reduction, and in that case, the appropriate electrochemical models can also be different. Some pathways relevant to this work are shown in Figure 3.1 as pathways (a) through (d), and some relevant equivalent circuits are shown in Figure 3.2 as circuits (a) through (d).

Circuit (a) corresponds to pathway (a) and has been previously derived in detail.[26]

Circuit (b) was used for LSM in previous chapter, and is shown here for comparison purposes only.

Circuit (c) is used for LSC in this work, and is obtained from circuit (b) by adding the assumption that ion conduction in the mixed conductor is also fast ($R_{ion} \approx 0$). The circuit then simplifies, since the three capacitors can be summed in parallel, such that $C_{total} = C_{chem} + C_{ion}^{s} + C_{eon}^{p}$.

Circuit (d) is used for SNB in this work, and is an empirical circuit that corresponds to pathways (c) or (d),

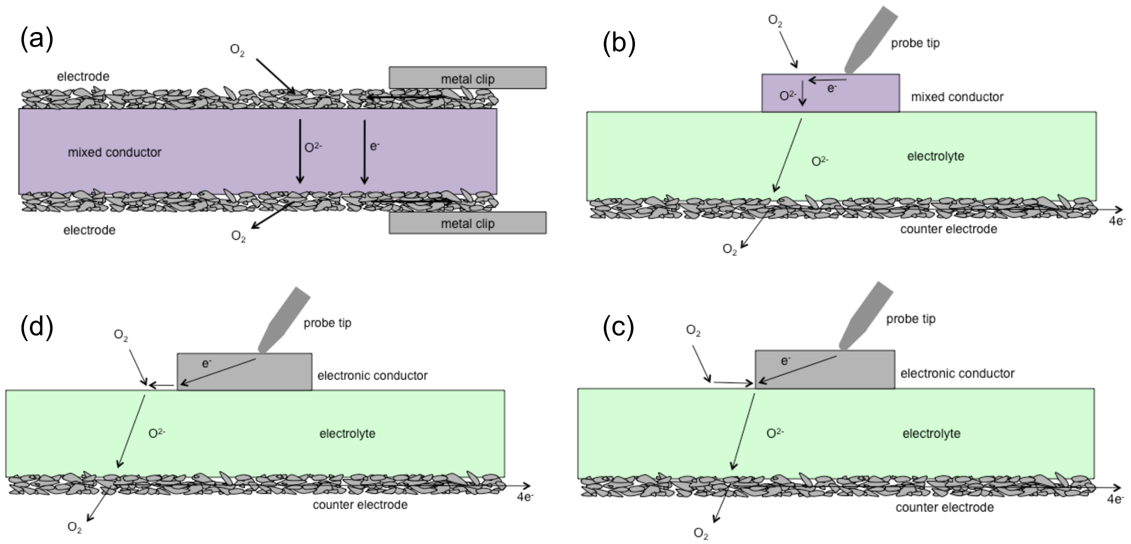

Figure 3.1. Possible electrochemical pathways. (a) mixed conducting pellet, (b) mixed conducting microelectrode, (c) electronically conducting microelectrode with surface diffusion on electrolyte, and (d) electronically conducting microelectrode with electron migration through electrolyte.

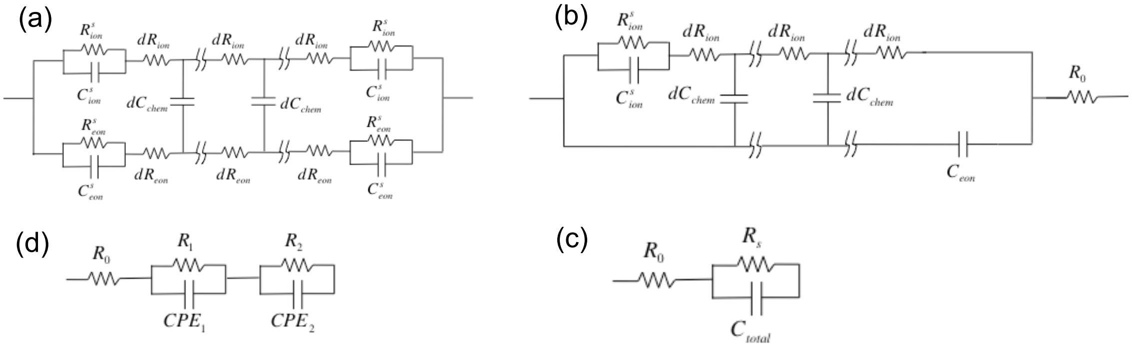

Figure 3.2. Equivalent circuits for (a) mixed conducting pellet, (b) $La_{0.5}Sr_{0.5}CoO_3$ microelectrode, (c) $(La_{0.8}Sr_{0.2})_{0.95}MnO_3$ microelectrode, and (d) Pt microelectrode on $Sr_{0.06}Nb_{0.06}Bi_{1.87}O_3$.

3.5 $La_{0.5}Sr_{0.5}CoO_3$ results

3.5.1 Structural characterization

All LSC films in this work were found by XRD to be (110) oriented as grown, and no additional reflections were visible. A typical set of XRD patterns taken prior to patterning is shown in Figure 3.3. AFM micrographs taken prior to patterning indicated the films have a columnar grain structure with ~ 50 nm - 100 nm column diameters, as shown in Figure 3.4, with a typical r.m.s. surface roughness of 3 nm. After patterning (*i.e.*, photolithography and ion milling), typical samples looked as shown in the optical photos in Figure 3.5.

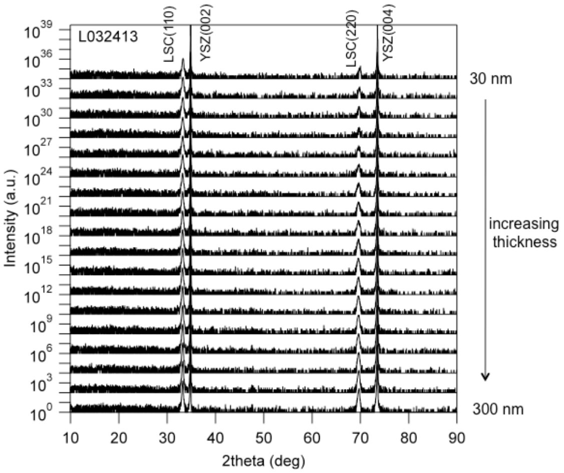

Figure 3.3. XRD patterns acquired from a single YSZ substrate containing $La_{0.5}Sr_{0.5}CoO_3$ films with thicknesses in the range 30 nm - 300 nm. Courtesy of Shingo Maruyama.

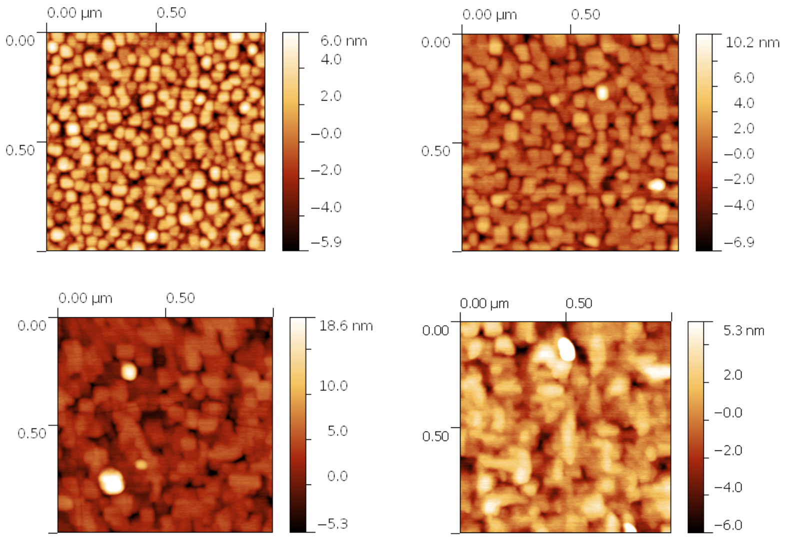

Figure 3.4 $La_{0.5}Sr_{0.5}CoO_{3-\delta}$ films as grown by PLD with thicknesses of 30 nm (upper left), 84 nm (upper right), lower left (192 nm), and lower right (300 nm). Courtesy of Shingo Maruyama.

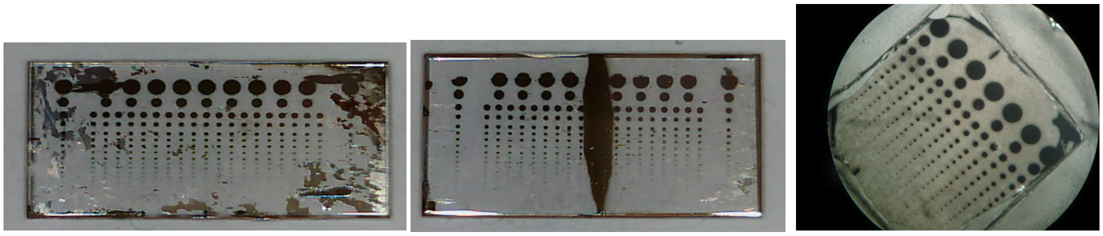

Figure 3.5. Optical photos of typical LSC samples. From left to right: various thicknesses ranging from 300 nm - 30 nm; a sample containing exactly two film thicknesses, 300 nm and 30 nm; and uniform 200 nm thickness. Some dark smudges are visible; this is residual silver paste on the backside of the transparent substrate (used to affix the substrate during deposition).

Optical microscopy, AFM, and SEM indicated that the microelectrode dimensions were precise and repeatable. The microelectrode diameters were consistently a few microns smaller than nominal, and the edges exhibited a few microns of waviness, resulting in ~ 5% variation in area between nominally identically microelectrodes. The film thickness was uniform within a few nanometers across a given microelectrode. A height "blip" was typically observed by AFM at the edges of a given microelectrode, suggesting that a small amount of material debris collected at the dot edge during the milling process. These findings are illustrated in Figure 3.6.

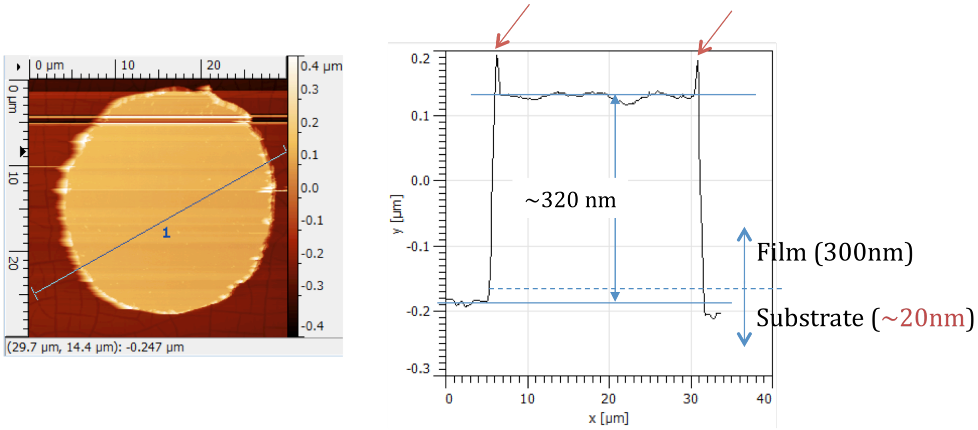

Figure 3.6. AFM profile scan of an LSC microelectrode with 300 nm nominal thickness, 30 um nominal diameter. Courtesy of Shingo Maruyama.

Some previous reports have used wet etching with hydrochloric acid to pattern oxide films, and these reports find that the acid undercuts the photoresist by ~ 20 um. By contrast, the dry etching (ion milling) technique used here exhibits only 2 um - 3 um undercutting as illustrated by SEM and AFM in Figure 3.7, resulting in sharper edges and improved thickness uniformity.

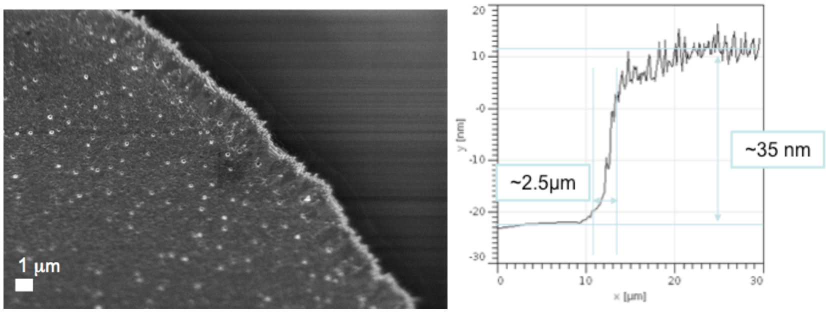

Figure 3.7. Edge quality of LSC films after patterning by ion milling. Left: SEM micrograph, taken from a sample without carbon coating. Right: AFM profile scan, courtesy of Shingo Maruyama.

Two potential problems were revealed by high magnification SEM imaging. First, most of the patterned films had numerous nanoscale cracks, as seen in Figure 3.8. Such cracks were also seen by AFM prior to patterning. These cracks were undoubtedly caused by the fast 100°C/min cooling rate that was used after deposition. Such a fast cooling rate should be avoided when processing films of materials like LSC that exhibit high thermochemical expansivity. Second, as discussed in Chapter 1, SEM images acquired from these films after impedance testing revealed that numerous silver particles had accumulated on the film surfaces during testing. See Figure 3.9. The implications of these two potential problems are addressed below in the interpretation of the impedance results.

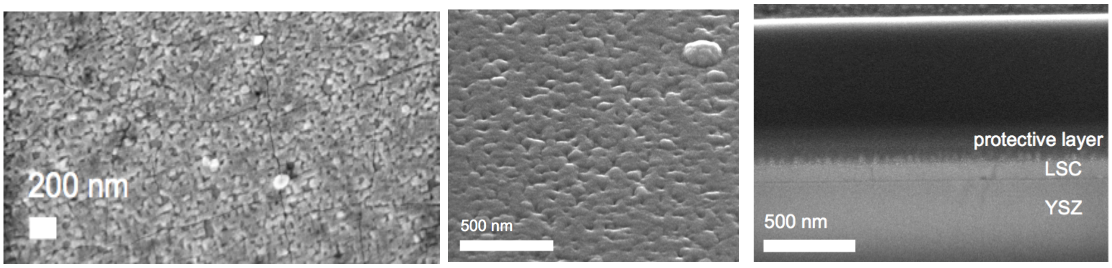

Figure 3.8. Surface and cross-section SEM micrographs of a representative $La_{0.5}Sr_{0.5}CoO_{3-\delta}$ film with 100 nm thickness that did not undergo impedance testing. Sample is tilted 52° in the center and right images.

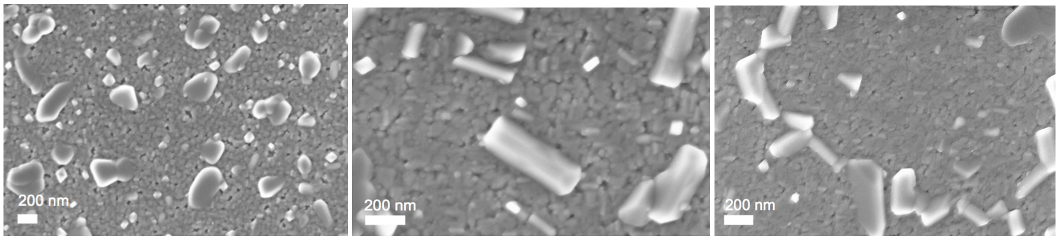

Figure 3.9 SEM micrographs acquired after impedance testing of $La_{0.5}Sr_{0.5}CoO_{3-\delta}$ films with thicknesses of 30 nm (left), 165 nm (middle), and 300 nm (right).

3.5.2 Impedance data

Representative electrochemical impedance spectra acquired from the LSC films are shown in Figure 3.10. Each spectrum consists of a single undepressed arc that coincides with the real axis at high frequencies. The characteristic frequency of the arc (*i.e.*, the frequency at which the imaginary component is most negative) decreased with decreasing temperature, decreasing pO2, and increasing thickness. Each spectrum was fit to the equivalent circuit described in Section 3.3.

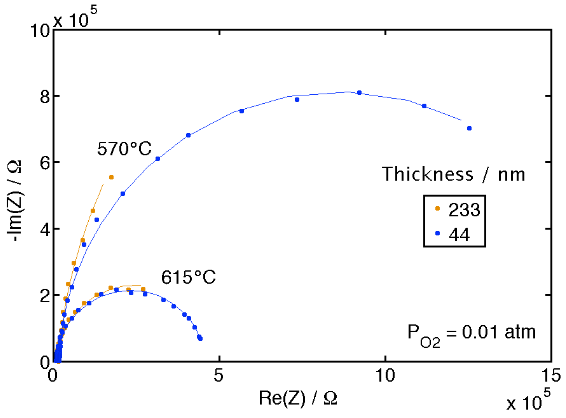

Figure 3.10. Typical impedance spectra acquired from thin film $La_{0.5}Sr_{0.5}CoO_{3-\delta}$ microelectrodes over the frequency range 10 kHz - 20 mHz. Points are the raw data; Curves are fits to the equivalent circuit shown in Section 3.4. The data shown here were acquired from microelectrodes with 200 μm diameter at the indicated temperatures and oxygen partial pressure.

A total of 680 impedance spectra were acquired in this experiment over the course of 5 days. Each spectrum yielded three fit parameters: an offset resistance R_0, a total capacitance C_{chem}, and a surface resistance R_s. These fit parameters are plotted in Figure 3.11, Figure 3.12, and Figure 3.13.

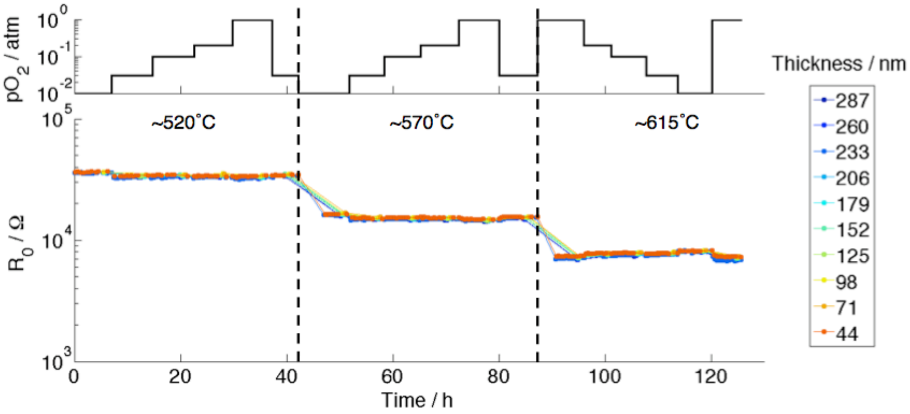

Figure 3.11. Offset resistance R_0 extracted from impedance spectra measured from $La_{0.5}Sr_{0.5}CoO_{3-\delta}$ films of various thicknesses at the indicated temperatures and oxygen partial pressures.

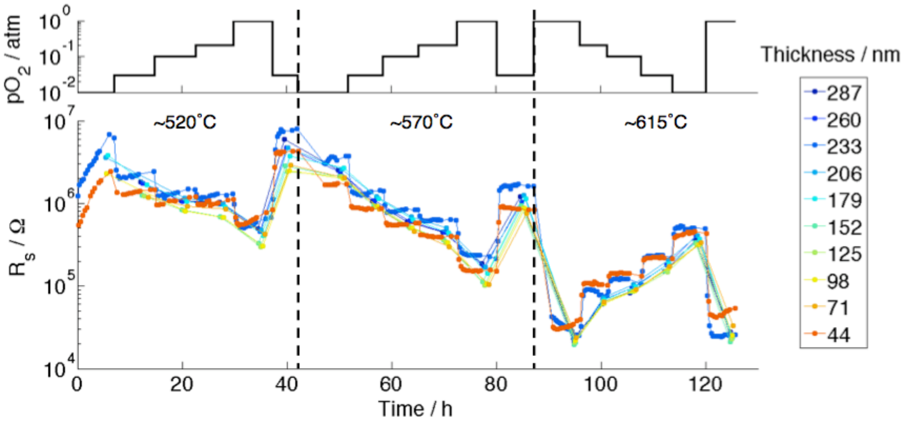

Figure 3.12. Surface resistance R_s extracted from impedance spectra measured from $La_{0.5}Sr_{0.5}CoO_{3-\delta}$ films of various thicknesses at the indicated temperatures and oxygen partial pressures.

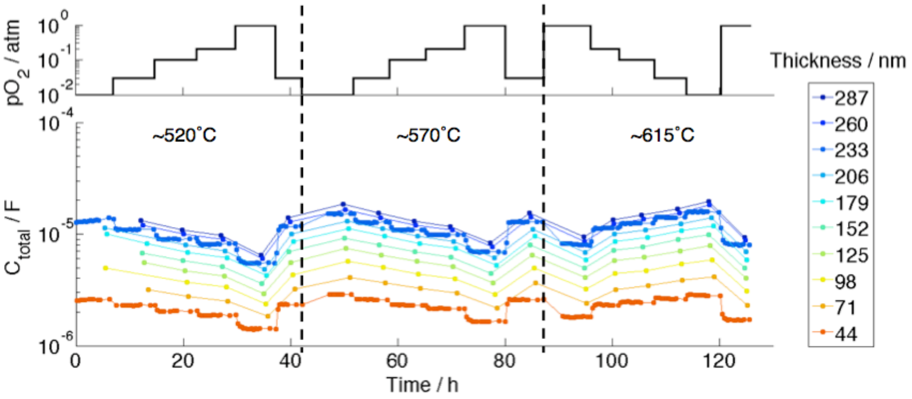

Figure 3.13. Total capacitance C_{chem} extracted from impedance spectra measured from $La_{0.5}Sr_{0.5}CoO_{3-\delta}$ films of various thicknesses at the indicated temperatures and oxygen partial pressures.

The surface resistances R_s were initially unstable. Over the first 40 hours of measurement at ~520˚C, they increased by more than an order of magnitude. The degradation rate appeared to be independent of film thickness, and it slowed over time, such that the resistances approximately stabilized after several tens of hours. Data from a second sample (see Figure 3.14) confirmed that this initial degradation is approximately linear with time for the first few days, independent of thickness, and independent of how often the microelectrode was probed, indicating that the repeated probing is not causing the degradation. Overall, the surface resistance of the films from both samples degraded by roughly a factor of 50 before stabilizing.

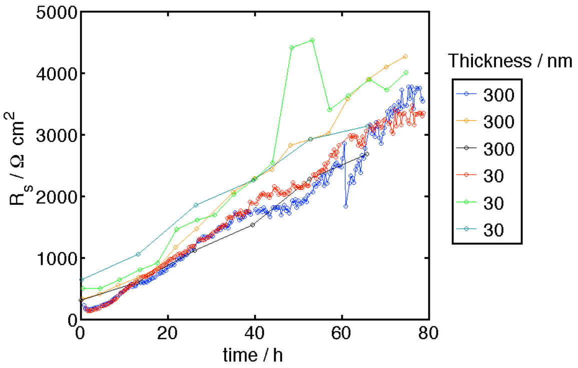

Figure 3.14. Surface resistance measured on a second sample of LSC microelectrodes with thicknesses of 30 nm and 300 nm, probed at ~ 520˚C in 0.01 atm O_2.

Returning to the primary sample, at first glance the total capacitances C_{chem} appear stable. Close inspection reveals that the total capacitances of the 233 nm and 300 nm films appear to have increased by 10-20% over the first 40 hours, while the total capacitances of the 30 nm and 44 nm films remained stable. The cause of this difference in stability is unknown.

The offset resistances R_0 were stable, dependent on temperature, and only very weakly dependent on thickness and oxygen partial pressure. These findings are consistent with the attribution of the offset resistance primarily to ion conduction through the YSZ electrolyte.

The thickness dependence of these three fit parameters at 615°C is shown in Figure 3.15. The surface resistance R_S shows no thickness dependence to first order. This finding indicates that the sidewalls of any pores or nanoscale cracks in the films contribute negligibly to the surface activity. The offset resistance R_0 depends slightly on oxygen partial pressure and increases very slightly as thickness decreases, suggesting that sheet resistance (electronic conduction) through the LSC makes a measurable but very small contribution to the offset resistance. The total capacitance C_{total} is proportional to thickness, and by extrapolating to zero thickness, the interfacial capacitance can be estimated as being small, less than 0.01 F/cm^2.

Two second-order effects are noteworthy. First, the fit residuals for the surface resistance and chemical capacitance share a systematic trend with thickness. This trend is consistent with steady-state temperature variations of an estimated ±8°C across the nominally isothermal stage (estimated from the Arrhenius slopes in

Figure 3.17). Second, the extrapolated total capacitance fits do not coincide at zero thickness. One possible explanation is that the surface divots in the LSC film decrease the volume of the outermost nanometers of the film and effectively introduce error in the film thickness.

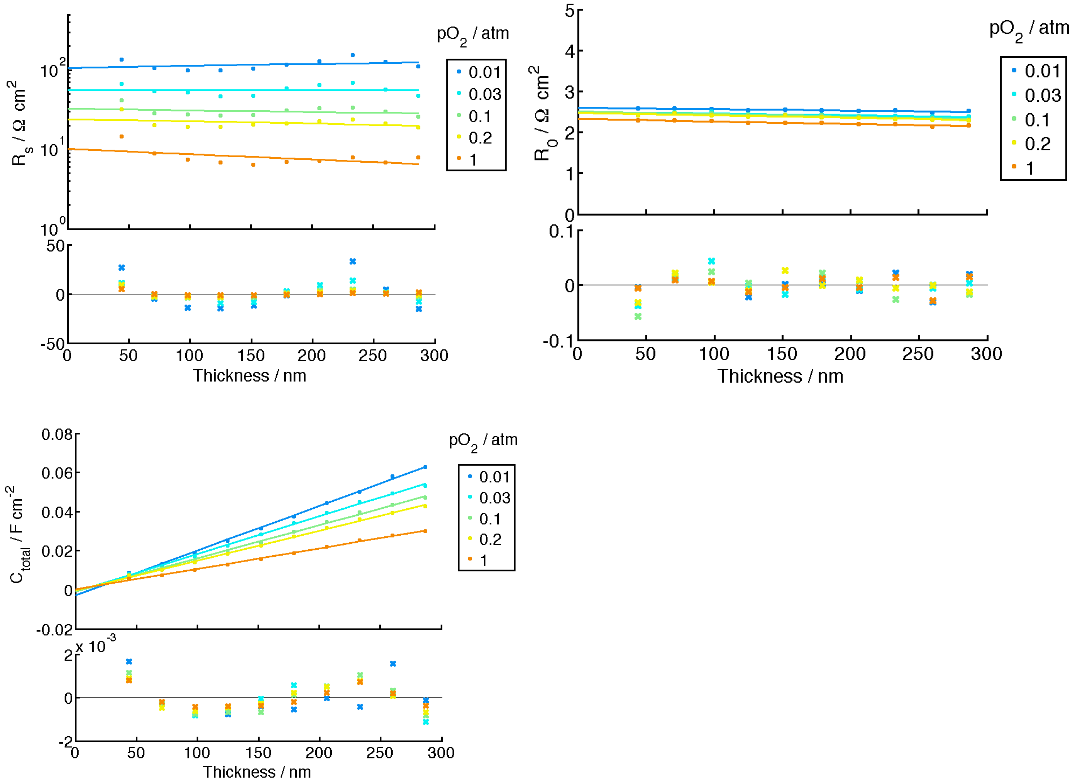

Figure 3.15. Area-normalized surface resistance R_s (upper left), total capacitance C_{total} (lower left), and offset resistance R_0 (upper right) of (200 μm diameter) $La_{0.5}Sr_{0.5}CoO_{3-\delta}$ microelectrodes of various thicknesses at 615°C. Lines are linear fits to the raw data points. The fit residuals are plotted as a subplot below the main plot.

The slope of total capacitance with thickness is equivalent to the volume-normalized chemical capacitance. These values are plotted in Figure 3.16 alongside comparable values reported in the literature for bulk samples of the same LSC composition. The chemical capacitance appears to be significantly lower in the films than in bulk samples. This difference may stem from the fact that grain boundaries occupy a high volume fraction in the films relative to bulk samples. Segregation of Sr to the film surface (as has been observed in LSM[58]) would also be expected to lower the chemical capacitance of the films.

In Figure 3.17, the surface resistance of the films is plotted versus oxygen partial pressure and versus temperature in Arrhenius form. Strikingly, the activation energy between 570˚C and 615˚C is 2.5 eV, nearly identical to what was measured previously on equilibrated films of $Ba_{0.5}Sr_{0.5}Co_{0.8}Fe_{0.2}O_{3-\delta}$ (BSCF) films grown on SDC(100) / YSZ(100) (Francisco Barroso, Haile group unpublished), and the absolute magnitudes of the surface activities are also quite similar.

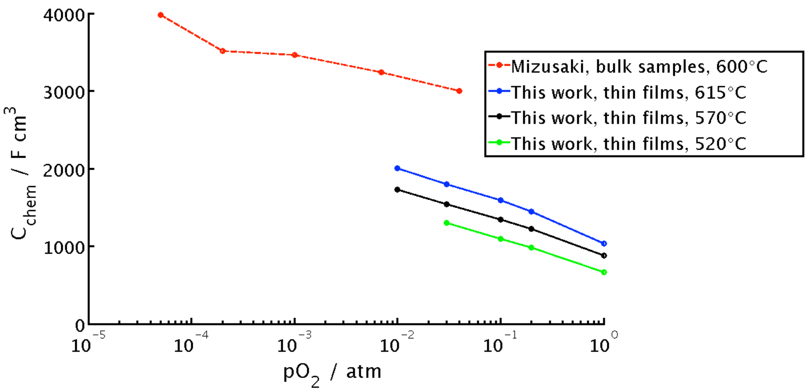

Figure 3.16. Comparison of the volume-normalized chemical capacitance of thin films (this work) and bulk samples[59] of $La_{0.5}Sr_{0.5}CoO_{3-\delta}$. Lines connecting the data points are guides for the eye.

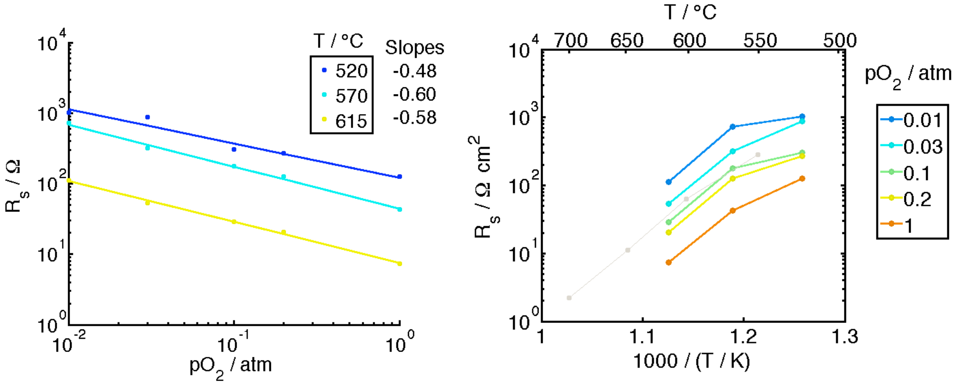

Figure 3.17. Surface resistance R_s of $La_{0.5}Sr_{0.5}CoO_{3-\delta}$ films after dwelling several hours at each given temperature and oxygen partial pressure, plotted versus oxygen partial pressure (left) and in Arrhenius form (right). Points were calculated by averaging the values measured from several film thicknesses. For comparison, data at 0.2 atm for $Ba_{0.5}Sr_{0.5}Co_{0.8}Fe_{0.2}O_{3-\delta}$ films (grown on SDC (100) on YSZ (100)) are shown at right in light gray (Francisco Barroso, Haile group unpublished).

3.6 $Sr_{0.06}Nb_{0.06}Bi_{1.87}O_3$ results

3.6.1 Structural characterization

Optical and SEM images of platinum microelectrodes on an SNB substrate are shown in Figure 3.18. The microelectrodes are ~ 600 nm thick. As a result of the photolithography liftoff process, the outermost ~ 2 microns of each microelectrode are slightly thicker than the rest of the microelectrode. The diameters were measured by optical microscopy and found to be close to the nominal values.

After testing, the surface of the SNB was observed to have became rough and faceted, and bismuth-rich particles were accumulated atop the grain boundaries of the SNB, as shown in Figure 3.19. These findings indicate that SNB is not fully stable under the testing conditions. The platinum microelectrodes exhibited some coarsening as a result of the SNB surface faceting, and some Ag was detected on the platinum. A few microelectrodes that were probed, including the one shown in Figure 3.19, were observed to have blisters. These are attributed to oxygen evolution at the platinum-SNB interface driven by repeated impedance measurements.

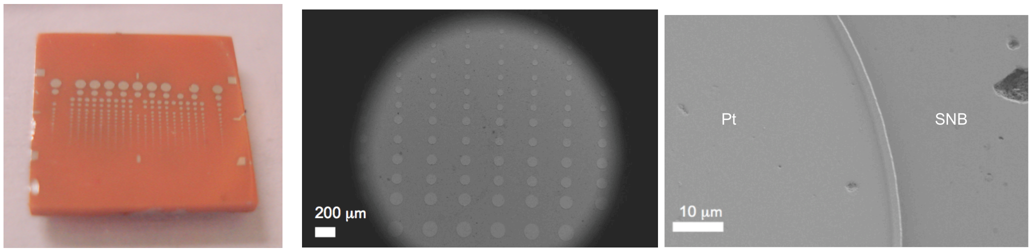

Figure 3.18. Optical (left) and SEM (right) images of platinum microelectrodes on an SNB substrate, before impedance testing.

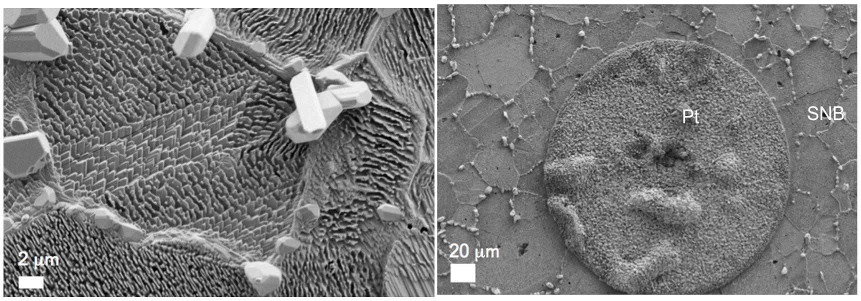

Figure 3.19. SEM images of the SNB surface (left) and a platinum microelectrode (right) after several days of impedance testing at 575°C - 650°C under $pO_2 = 10^{-3}$ - 1 atm.

3.6.2 Impedance spectra

Typical impedance spectra acquired from the platinum microelectrodes are shown in Figure 3.20. The spectra are well-fit by the empirical equivalent circuit described in Section 3.4.

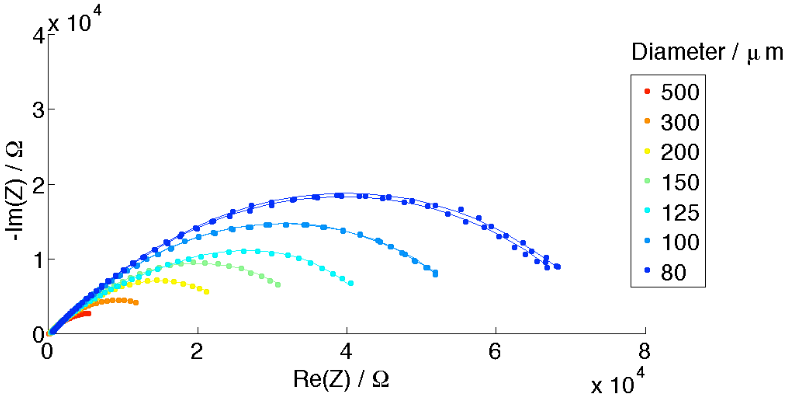

Figure 3.20. Impedance spectra acquired from platinum microelectrodes of various diameters on SNB at ~ 625°C in 0.2 atm O_2. Points are raw data; lines are fits to the empirical equivalent circuit described in Section 3.4.

The overall arc width R_{dc} - R_0 and the offset resistance R_0 are plotted in Figure 3.21. R_{dc} - R_0 (*i.e.*, the overall arc width, Z(0 Hz) - Z(∞ Hz)) is equivalent to the electrochemical reaction resistance R_s under the assumption that in SNB the transference number for ions $t_{ion} \geq 0.999$. This assumption is consistent with a previous report on doped bismuth oxide [9] but requires further verification.

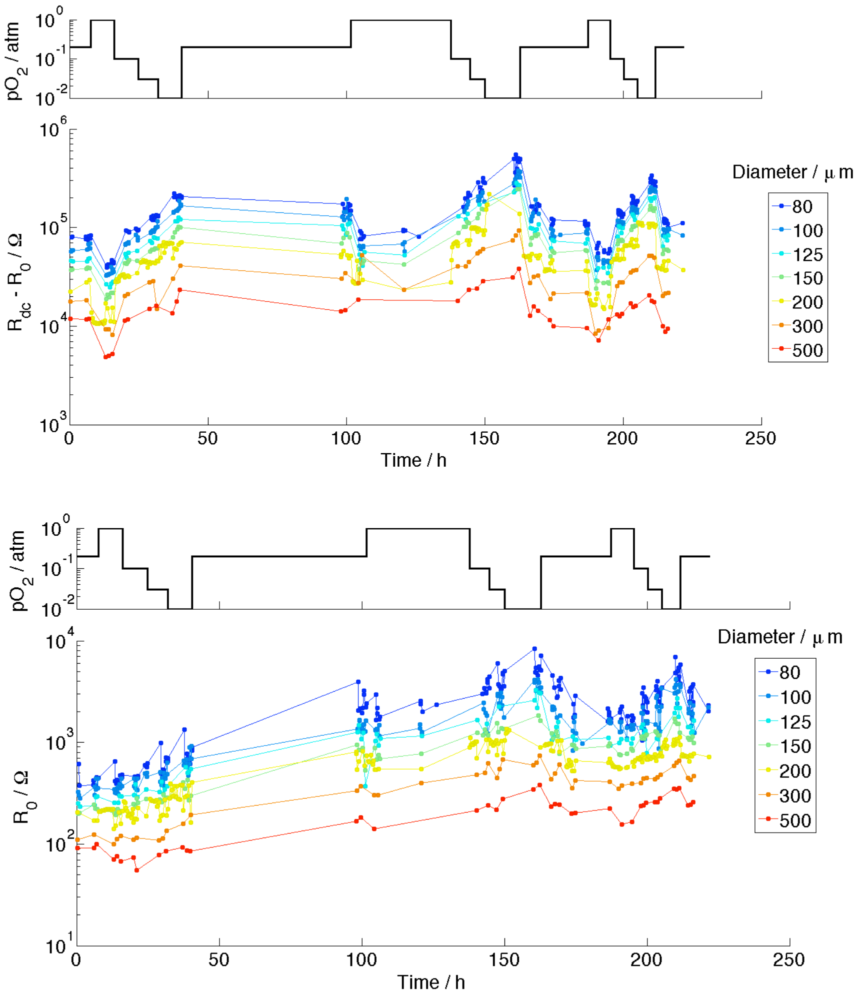

Figure 3.21. Overall arc width R_{dc}-R_0 (top) and offset resistance R_0 (bottom) measured over time at the indicated temperatures and oxygen partial pressures from platinum microelectrodes of various diameters on SNB. Points were extracted from the impedance spectra; lines connect the points as guides for the eye.

The diameter dependence of the electrochemical reaction resistance is plotted in Figure 3.22 at left. The slope of close to -1 in the double-logarithmic plot indicates that the electrochemical activity scales with the microelectrode perimeter. This important finding is distinct from the LSC and LSM films discussed above; it indicates that the electrochemical reaction proceeds via a triple phase boundary path. It also rules out dissociative adsorption on the platinum microelectrodes as a rate-limiting step, since that process would be expected to scale with surface area. The same data is plotted versus oxygen partial pressure in Figure 3.22 at right. The slopes here indicate that the electrochemical activity scales with $pO_2^{-0.3}$. This value is close to the -0.25 that would be expected if electron migration at the SNB surface were the rate-limiting step.

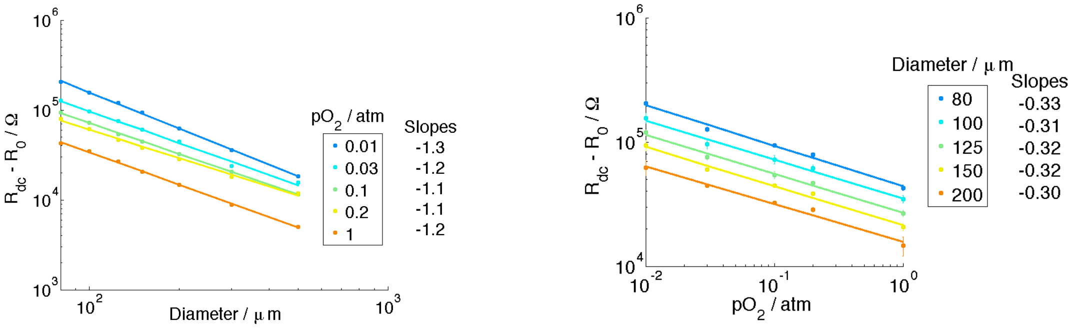

Figure 3.22. Overall arc width R_{dc}-R_0 measured from platinum microdots on SNB at ~625°C as a function of diameter (left) and oxygen partial pressure (right). Points were extracted from the impedance spectra; lines are linear fits on a double-logarithmic scale.

Figure 3.20, Figure 3.21, and Figure 3.22 all assume that the microelectrodes are at the same indicated temperature. In practice, tip cooling lowers the average surface temperature of smaller-diameter microelectrodes to a greater extent. As discussed in Chapter 1, a knowledge of the cooling-induced thermovoltage along with the SNB Seebeck coefficient enables the extent of the temperature drop due to tip cooling to be estimated. Using this temperature correction, an Arrhenius plot of the electrochemical reaction resistance is shown in Figure 3.23. Activation enthalpies are calculated from the slope of linear fits to these data, and are shown next to the legend. The measured activation energy of 0.9 eV - 1.0 eV agrees well with the activation energy of 1.1 eV measured by Takahashi for the electronic hole conductivity of a similar doped bismuth oxide composition. On the other hand, the activation energies measured for surface catalysis on platinum are different, 1.6 eV - 2.3 eV. Thus the temperature behavior is also consistent with electron migration through the bismuth oxide being the rate-limiting step.

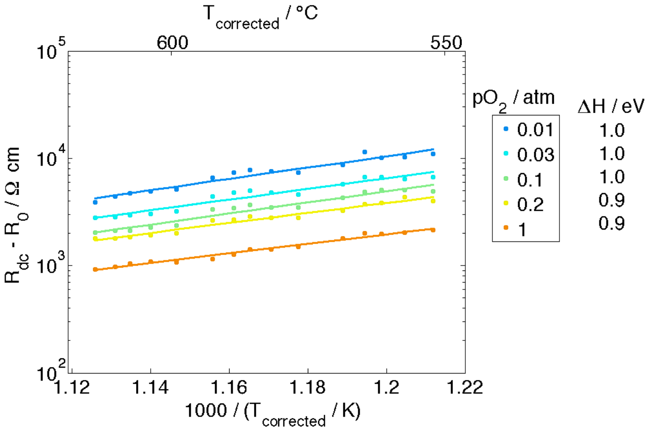

Figure 3.23. Arrhenius plot of the electrochemical reaction resistance. The film temperatures were corrected approximately for tip cooling. Points are extracted from the impedance spectra; lines are linear fits to the points. The activation enthalpy extracted from the line slopes is shown beside the legend.

3.7 Conclusions

For $La_{0.5}Sr_{0.5}CoO_3$ films on (100) YSZ, the impedance spectra in the measured temperature range 520˚C - 615˚C consisted of a single semi-circle. The measured capacitance and resistance values were unstable for the first ~ 50 h at 520˚C, and subsequently stabilized at higher temperatures. This stability suggests that silver particles (which continued to accumulate slowly on the sample surfaces during the high temperature measurements) do not significantly enhance or degrade the film activity. The thickness independence of the arc resistance R_s confirmed that bulk transport makes a negligible contribution, and suggested (since the density of surface grain boundaries exhibited some thickness dependence) that surface grain boundary sites are not significantly more active than other surface sites. The arc resistance was attributed entirely to the surface process, under the assumption that the LSC-YSZ interface was reversible for ion transport. The chemical capacitance of the LSC films scaled linearly with thickness, was stable over time, and was lower than the chemical capacitance of bulk $La_{0.5}Sr_{0.5}CoO_{3-\delta}$ samples reported in the literature. The strikingly similar activity and activation energy between the $La_{0.5}Sr_{0.5}CoO_3$ films measured in this work and $Ba_{0.5}Sr_{0.5}Co_{0.8}Fe_{0.2}O_{3-\delta}$ macroscopic electrodes (1 cm^2) measured previously suggests that these two film compositions are rate-limited by the same process.

For platinum films on a doped bismuth oxide substrate, specifically $Sr_{0.06}Nb_{0.06}Bi_{1.87}O_3$, fitting the equivalent circuit to an empirical model enables a total resistance to be extracted. Under the assumption that the substrate has an ionic transference number > 0.999, this resistance could be equated with the electrochemical reaction resistance. The diameter, pO2, and temperature trends suggest that catalysis proceeds by a pathway involving dissociative adsorption onto the bismuth oxide, followed by diffusion towards the triple phase boundary and/or surface incorporation. The activation energy of the total resistance was quite similar to the previously reported activation energy for electronic hole conduction in yttria-doped bismuth oxide, suggesting that electron migration is rate-limiting. Overall, the high activity near the metal-doped-Bi_2O_3 interface suggests that using such materials in a cathode with a favorable microstructure should be competitive with other state of the art cathodes. These measurements should be repeated in an electron-blocking configuration (*e.g.*, doped bismuth oxide films on a YSZ substrate) to confirm that electronic leakage through the substrate is not significant.